An MR-Compatible Haptic Interface With Seven Degrees of Freedom

Markus Kühne , Martin Eschelbach , Ali Aghaeifar , Lisa von Pflugk, Axel Thielscher, Marc Himmelbach, Klaus Scheffler, Patrick van der Smagt, and Angelika Peer

Abstract—**Functional magnetic resonance imaging (fMRI) is a powerful tool for neuroscience. It allows the visualization of active areas in the human brain. Combining this method with haptic interfaces allows one to conduct human motor control studies with an opportunity for standardized experimental conditions. However, only a small number of specialized MR-compatible haptic interfaces exist that were mostly built around specific research questions. The devices are designed for pure translational, rotational, or grasping movements. In this work, we present a novel MR-compatible haptic interface with seven degrees of freedom (DoF), which allows for both translations and rotations in three DoF each, as well as a two-finger precision grasp. The presented haptic interface is the first one with these capabilities and is designed as a universal tool for human motor control studies involving fMRI. It allows for the switching of the paradigm to reprogramming rather than redesigning when moving on to a new research question. We introduce its kinematics and control, along with results of MR compatibility tests and a preliminary fMRI study, showing the applicability of the device.**

Index Terms—**Magnetic resonance imaging (MRI), robot kinematics, robots.**

M. Kühne is with the Technical University of Munich, München 80333, Germany (e-mail: Markus.Kuehne@tum.de).

M. Eschelbach and A. Aghaeifar are with the Max-Planck Institute for Biological Cybernetics, Tübingen 72076, Germany.

L. von Pflugk is with the Institute for Innovation and Change Methodologies, Munich 80331, Germany.

A. Thielscher is with the Danish Research Center for Magnetic Resonance, Copenhagen University Hospital Hvidovre, and also with the Technical University of Denmark, Kopenhagen 2800, Denmark.

M. Himmelbach is with the University of Tübingen, Tübingen 72074, Germany.

K. Scheffler is with the the Max-Planck Institute for Biological Cybernetics, Tübingen 72076, Germany, and also with the University of Tübingen, Tübingen 72076, Germany.

P. van der Smagt is with Data Lab, Volkswagen Group, München 80805, Germany.

A. Peer is with the Free University of Bozen-Bolzano, Bolzano BZ 39100, Italy.

I. INTRODUCTION

HAPTIC interfaces are robotic systems that create a sense of touch by applying haptic feedback to an operator. They yield the ability to not only see but also "feel" virtual environments. In human motor control studies using functional magnetic resonance imaging (fMRI), they can serve as a tool to introduce standardized experimental conditions. But up to now, devices were built around specific research questions, and no general device exists that allows for the targeting of a series of these research questions by just reprogramming rather than redesigning. The magnetic field poses a series of challenges to the construction of robotic systems to be placed in MR environments: Ferromagnetic components and floating actuators lead to safety issues and create image artifacts. The motion capabilities or degrees of freedom (DoF) of existing MR-compatible[1] haptic interfaces are limited. In our previous work [1], we presented existing MR-compatible haptic interfaces with one to three DoF. The devices allow for individual movements like reaching with the arm or finger, grasping, or wrist rotations. Actuation principles vary from remotely located dc-motors, over pneumatic and hydraulic actuators as well as electrostatic motors, to ultrasonic motors (USMs). The advantages and disadvantages of these actuation principles were discussed in [2]. The state-of-the-art has been extended since, and recent key developments were an MR-compatible gripper [3] as well as a wrist mechanism [4]. Both of the devices provide one DoF and are based on cable transmissions from a remotely located dc motor. Moreover and similar to our own previous work of a device with three DoF [2], the soft-wrist [5], which is an MR-compatible device with two DoF actuated by USMs, has been presented. Recently, a device with five DoF, called the HFI-5 [6], was developed by Stanford University. Still, most devices are specialized for a subset of possible Cartesian motions and there is no universal device. Such a device, however, would allow for the switching of the paradigm to reprogramming rather than redesigning when moving on to a new research question. Since neuroscientists are not typically mechanical or control engineers, this should help them in setting up studies more easily, while also saving time and monetary resources. Moreover, complex tasks involving natural, unconstrained pick-and-place motions can be targeted. In our previous work [1], we already presented a first concept for a universal MR-compatible haptic interface. However, this

[1]For an exact definition and use of the term *MR-compatible* in this work, the interested reader may refer to [10].

concept has not been realized since improvements on both kinematics and control algorithms had to be determined. Moreover, only one sensor-actuator unit was tested for MR-compatibility and no fMRI study was carried out with the device.

The realized novel MR-compatible haptic interface with seven DoF relies on a recently developed Octopod kinematics. This kinematics provides six DoF and was already conceived for a later application in MR environments [7]. A haptic gripper [8] actuated via Bowden cables is additionally mounted on the end effector. The components have been carefully selected and iteratively tested to ensure a low magnetic susceptibility. Moreover, all actuators are nonfloating in order to avoid image artifacts. USMs drive the haptic interface and they are controlled by a newly proposed hybrid sliding mode controller (SMC) [9]. The controller allows for both high and low velocities for a motor that only generates high velocities by default. The ability to provide low velocities is essential, since those often occur in haptic applications. The whole system has been extended with an MR-compatible support frame so that it is ergonomic, safe, and can be quickly deployed for fMRI studies. Moreover, a software interface to the open source haptic rendering software Chai3D allows for the creation of a variety of task scenarios. Experiments were carried out in order to validate the bi-directional MR compatibility, in such a way that neither image quality nor device performance is impaired by the magnetic field.

This paper is structured as follows: Section II specifies the design criteria, whereas Sections III and IV detail the hardware design and haptic rendering of the prototype, respectively. The applied performance indices are presented in Section V along with results of an evaluation. The MR-compatibility is validated in Section VI. Finally, the results are discussed and a conclusion is drawn in Sections VII and VIII.

II. DESIGN CRITERIA

We would like to design our device for unconstrained pick-and-place tasks, for the first time allowing one to characterize brain processes that underlie natural reach-to-grasp movements. This extends the types of questions in the field of visuomotor control that can be asked by neuroimaging [11]. Providing the possibility of such an unconstrained motion means that the device disposes of seven DoF. This covers all possible Cartesian motions of the human hand, including the possibility of rotations and a two-finger precision grasp. With such a device, specialized subtasks like reaching or lifting objects can also be rendered.

Minimum output capabilities have to be met along all DoF and a broad range of these have been defined for haptic interfaces by Fischer *et al.* as early as 1990 [12]. They include minimum velocities, accelerations, available workspace, and others. As a complement to these requirements, a typical pick-and-place experiment provides the minimum required torques, as well as lift and grasp forces. Light objects, comparable to a glass of water, should be manipulated. Thus, we can approximate the order of magnitude of the weight as well as inertia of the objects, and thus forces and torques, to be rendered. An empty glass of water has a weight of approximately $m_{glass} = 0.2 \, kg$ and a maximum inertia of $I_{glass} = 1\,000 \, kg \cdot mm^2$, as in Table I.

TABLE I
PARAMETERS OF A TYPICAL PICK-AND-PLACE EXPERIMENT FOR OUR DEVICE, LIFTING A LIGHT OBJECT SUCH AS A GLASS OF WATER

mass, inertia ·	maximum acceleration =	maximum force, torque
0.2 kg	9.81 m/s^2	1.96 N
1000 kg·mm^2	15 000 deg/s^2	0.52 N·m

Forces and torques can be derived using Newton's second law of motion, $F = m \cdot a$.

Assuming a maximum acceleration of $a_{trans} = 9.81 \, m/s^2$ [12] and the peak angular acceleration of the human wrist of $a_{rot} = 15\,000 \, deg/s^2$ [13], we obtain a maximum force $F_{max} = 1.96 \, N$ and torque $\tau_{max} = 0.52 \, N \cdot m$ to be rendered. This allows deriving the grip force. It depends mainly on the object weight and the friction coefficient. From literature, we know that the correlation of the static grip force with the object weight is approximately linear [14]. Also, the correlation of the maximum grip force with the inverse coefficient of friction μ is approximately linear with a safety margin F_{safety} [15]. Hence, the grip force can be approximated by

$$F_{grip} = F_{max} \cdot 1/\mu \cdot s + F_{safety}. \tag{1}$$

With $F_{max} = 1.96 \, N$, a friction coefficient of glass in a human hand $\mu_{glass} = 1.1$ [16], a safety margin $F_{safety} = 3 \, N$, and a slope of $s \approx 3$ [15], we obtain a grip force of $F_{grip} = 8.3 \, N$.

Besides these required output capabilities, the device should be compact enough so that it fits into the entry of the MR scanner bore. Moreover, it should be MR-compatible, safe, and ergonomic for long-lasting fMRI studies. Thus, the design requirements can be summarized as follows:

1) Seven actuated DoF at the end effector to allow for a versatile application as well as natural, unconstrained pick-and-place tasks, with rotations of $\pm 30°$ around all axes and a volume of operation of at least 300 mm^3 [12].
2) The minimum force, torque, and grip force output capabilities should be 1.96 N, 0.52 Nm, and $F_{grip} = 8.3 \, N$, respectively. In order to provide a realistic feeling, the minimum translational velocities and translational accelerations should be 1 m/s and 9.81 m/s^2, respectively [12].
3) Compact design so that the device fits into the entry of the MR scanner bore. For our first application, this is a 3-T MRI system (Prisma, Siemens; Erlangen, Germany) with a scanner bore of 60 cm in diameter.
4) Bi-directional MR compatibility of the entire system should be provided: Neither image artifacts should occur, nor position control precision should be affected by the MR environment.
5) Safe and ergonomic usage of the device should be provided so that subjects can perform natural motions, even in long-lasting fMRI studies.

III. HARDWARE DESIGN

The realized system, called MR-Octo, is based on an Octopod kinematics, extended with a haptic gripper.
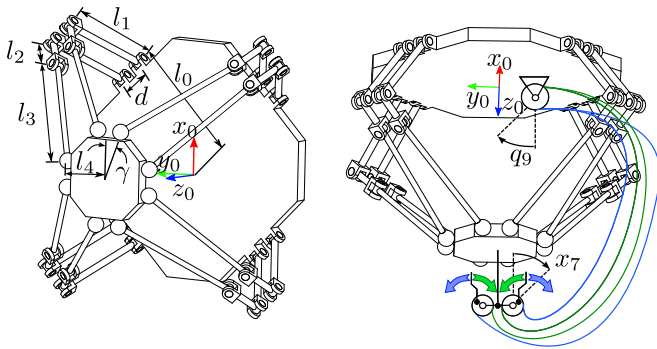
Fig. 1. Octopod kinematics providing six DoF (left) and Octopod kinematics augmented with schematic haptic gripper, driven by Bowden cables (right).
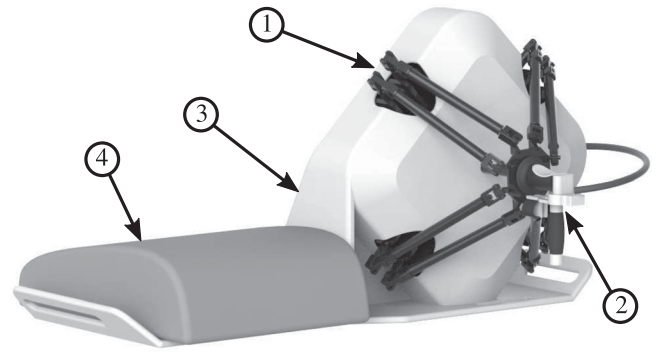

Fig. 2. MR-Octo (1) for right-handed operation with haptic gripper (2), mounted on a support frame (3) that also carries an MRI pillow (4), supporting the subject's legs.

A. Octopod

The Octopod kinematics was particularly designed for an application in MR environments [7] and is depicted in Fig. 1. It employs eight RRRS legs and provides six DoF. Each leg consists of three rotational joints and one spherical joint, whereas only the first rotational joint is actuated. All actuators are nonfloating and thus, remain stationary during movement of the end effector. This avoids image artifacts and decreases the inertia of moving components. In contrast to Hexapod kinematics, the Octopod kinematics also avoids singularities by design and thus has an increased dexterous workspace.

The kinematic parameters of the haptic interface are chosen consecutively and aim to meet our first three design criteria: First of all, distance d, length l_3, and angle γ are minimized, which improves the isotropy and output capabilities of the device, as already presented in our previous work [7]. Second, the overall compactness of the device is maximized, such that it fits into the entry of the MR scanner bore. The size of the actuation units ultimately determines the minimum realizable base radius l_0. Finally, lengths l_1, l_3, and l_4 are chosen in an iterative process that guarantees both workspace and minimum output capabilities to be achieved. Typically, a compromise between force/torque and velocity capabilities has to be made, given a certain set of actuators. For this first prototype, no formal optimization was carried out and lengths l_1, l_3, and l_4 were determined by the designer.

The resulting kinematic parameters of the MR-Octo are $l_0 = 0.17$ m, $l_1 = 0.08$ m, $l_2 = 0.03$ m, $l_4 = 0.06$ m, $d = 0.02$ m, and $\gamma = 18.34°$. Moreover, the kinematics is oriented in such a way that gravity g acts along the negative x_0-axis. This distributes the weight of the kinematics equally among the eight actuators. The kinematics constitutes the basis of the MR-compatible haptic interface. A rendering of the complete CAD design is shown in Fig. 2.

The system is actuated by nine USMs of the type Shinsei USR60-E3NT. Ten optical encoders measure their position as well as the gripper's orientation. A Mini27 Titanium force/torque sensor with six DoF from ATI IA at the end effector measures interaction forces and torques.

Most structural components of the device are made from polyvinyl chloride (PVC), polycarbonate (PC), and copper. The latter has been selected due to its thermal conductivity as well

TABLE II
OVERVIEW OF COMPONENTS, THEIR MATERIALS AND THEIR MAGNETIC
VOLUME SUSCEPTIBILITY IN SI-UNITS

Component	Material	χ_v
Structural components of Octopod and frame	PVC	$-10.71 \cdot 10^{-6}$
Haptic gripper housing	PC	$-9.56 \cdot 10^{-6}$
Haptic gripper screws	Brass	112
Ball bearings	ZrO_2	-0.64
USM housing and stand	Copper	$-9.63 \cdot 10^{-6}$
Six DoF force/Torque sensor and screws	Titanium	$1.81 \cdot 10^{-4}$

as shielding capability. Since the USMs are driven via friction, the temperature rises during prolonged operation. Employing copper as the motor stand and housing material allows for the cooling of the USMs during operation, as recommended by the manufacturer. Further components are titanium screws as well as ceramic ball bearings. The employed components, their materials as well as their magnetic volume susceptibility are listed in Table II. The magnetic volume susceptibility allows for the classification of the level of magnetizability of the components. Diamagnetic materials ($\chi_v < 0$) are repelled by the magnetic field and paramagnetic and ferromagnetic materials ($\chi_v > 0$) are attracted by the magnetic field. As a reference, iron has a magnetic volume susceptibility of 2 00 000. The materials were chosen depending on the components' primary function, but also in light of their potential MR compatibility, which finally needs to be experimentally validated.

B. Haptic Gripper

The gripper was developed by Deakin University, Australia and is based on a concept by Zoran Najdovski [8]. In cooperation, an MR-compatible version has been realized and is employed in the haptic interface. The gripper uses Bowden-cable actuation and thus, can move in space in six DoF without being affected in its performance. Technically, two DoF can be actuated separately. For the presented prototype, both DoF are coupled in such a way that both tips of the gripper move simultaneously, as depicted in Fig. 1. The actuation unit, built by the authors of this paper, consists of a ninth USM and a simple pulley.
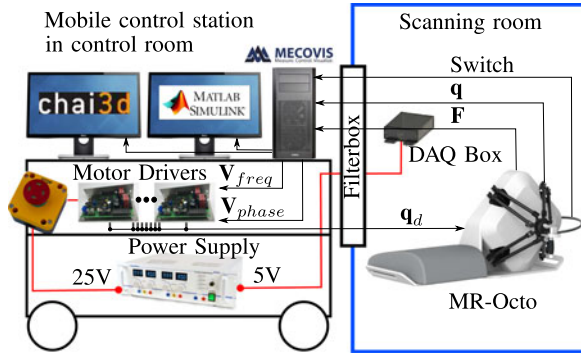
Fig. 3.   Signal flow between the mobile control station on wheels in the control room (left) and the scanning room (right). All signals are filtered as they pass from one room to the other.
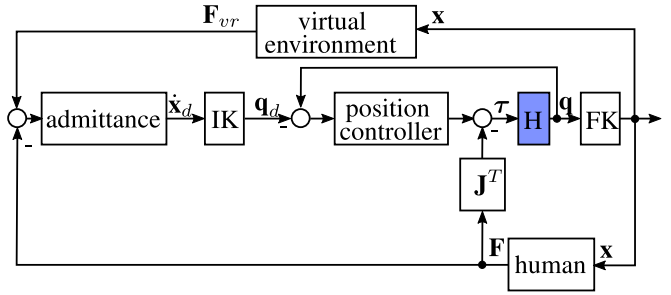

Fig. 4.   Admittance control scheme that determines the interaction of the haptic interface (H) with the virtual environment and the human operator. Forward kinematics (FK) and inverse kinematics (IK) transform between Cartesian and joint space. A low-level position controller sets the desired actuator positions.

C. Support Frame

The Octopod kinematics is mounted on a support frame as shown in Fig. 2. The support frame has been designed in order to provide an ergonomic, safe as well easy installation of the entire system. It is also made from MR-compatible materials, such as PVC and titanium. It allows for right-handed operation of the haptic interface and can be adjusted in two DoF, lengthwise and laterally to the proportions of each subject. On the left side of the support frame, an MRI pillow is placed that supports the subject's legs during long-lasting experiments.

IV. VISUAL AND HAPTIC RENDERING

The haptic rendering runs on a workstation and is implemented in Chai3D along with the visualization of the virtual environment. The haptic device is operated in admittance control mode.

A. Hardware and Software Setup

The haptic interface is connected to a workstation that executes control algorithms and performs visual and haptic rendering of a virtual environment. The signal flow between the MR-Octo and the workstation is depicted in Fig. 3. Commands to the motor drivers are computed via Matlab/Simulink and are executed by a Linux real-time kernel at a sampling rate of 1 kHz. Forward and inverse kinematics are solved by MotionGenesis Kane.

The communication with the hardware is managed via three Mecovis I/O cards. Those output two voltages, $V_{i,\text{freq}}$ and $V_{i,\text{phase}}$, in the range of $[-10; 10]$ V per motor i, in order to set the desired motor positions $\mathbf{q}_d$. The actual motor positions $\mathbf{q}$ as well as the measured forces and torques $\mathbf{F}$ are fed back to the workstation. The subject can also use a switch at the gripper to turn the haptic interface on or off. Signals are all transferred via shielded copper cables and no optical cables are employed.

B. Virtual Environment

The visual and haptic rendering of the virtual environment is performed in Chai3D [17]. Matlab/Simulink sends the end effector position $\mathbf{x}$ to Chai3D via a shared library. Chai3D computes interaction forces $\mathbf{F}_{vr}$ and sends them back using the same shared library.

C. Control of the Haptic Interface

The haptic interface is controlled via an admittance control scheme that determines the interaction with the human operator and the virtual environment. An overview is depicted in Fig. 4.

1) Admittance Control: Haptic interfaces are usually controlled by one of the two complementary control paradigms, impedance or admittance control. For impedance control, positions are measured and forces are commanded to the actuators. Conversely, for admittance control, forces are measured, whereas positions of the actuators are set. Since USMs are nonbackdriveable, admittance-type actuators, the admittance control paradigm has been adopted. Here, a minimal virtual mass $\mathbf{M}$ and damper $\mathbf{D}$ are rendered to keep the controller stable, and the resulting system can be written as

$$\mathbf{M}\ddot{\mathbf{x}}_d + \mathbf{D}\dot{\mathbf{x}}_d = \mathbf{F}_{vr} - \mathbf{F}. \tag{2}$$

Matrices $\mathbf{M}$ and $\mathbf{D}$ are diagonal 7×7 matrices with a virtual mass m_j and damping d_j for each DoF, respectively. Desired velocity $\dot{\mathbf{x}}_d$ and acceleration $\ddot{\mathbf{x}}_d$ of the end effector are 7×1 vectors, similar to the measured force $\mathbf{F}$ and the rendered force $\mathbf{F}_{vr}$. The force for all Cartesian DoF at the end effector is measured by the Mini27 Titanium force/torque sensor.

The haptic gripper requires force measurement for admittance control. The force applied at the gripper is a function of the gripper angle x_7 and the position of the ninth USM q_9, as depicted in Fig. 1, and the spring stiffness of the Bowden cables. With an approximation of the spring stiffness K, the exerted force at the gripper yields

$$F_{\text{gripper}} = K(q_9 - x_7). \tag{3}$$

In order to render a stiff contact with the virtual environment, we use the gripper orientation x_7 as an input to the virtually rendered impedance, instead of the actively controlled position q_9. Please note that q_9 is used for the low-level position control to avoid oscillations. These would result when using x_7, as it is a noncollocated variable with respect to its actuator USM 9. The principle is visualized in Fig. 5.
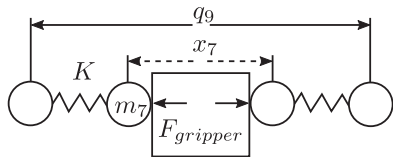
Fig. 5. Gripper principle, where approximated Bowden cable stiffness K, USM position q_9, and gripper orientation x_7 generate a grasp force F_{gripper}. Grasping an object also leads to a virtual reaction force $F_{vr,7}$, which is not depicted.
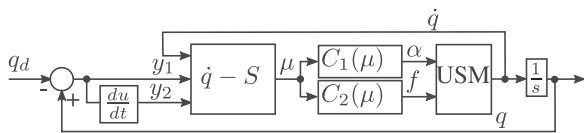

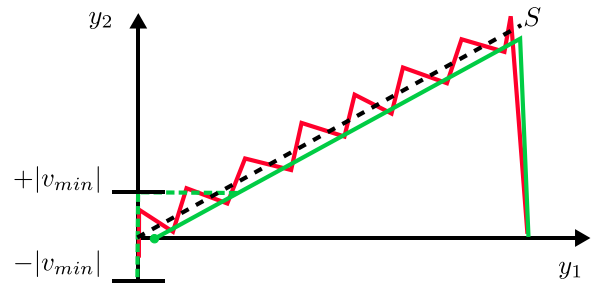Fig. 6. Hybrid SMC scheme for position control of a USM.

Fig. 7. Principle of the hybrid SMC in a phase portrait and after a step input: Ideal sliding surface S (dashed black), classical SMC (red), nonhybrid SMC (dashed green), and the proposed hybrid SMC (green).

2) Low-level Position Control: In order to realize the admittance control scheme, the employed USMs have to be foreseen with a low-level position control. However, commercial motor drivers do not allow for low velocities, which typically occur when interacting with haptic interfaces. In previous work [9], we have presented a hybrid sliding-mode control scheme that allows for both high and low velocities and is based on a second-order model of the USM. The actuation principle of USMs is based on the high-frequency vibration of a stator that is pressed against a rotor. The USM itself is composed of three major components: stator, rotor, and friction layer. The stator carries piezoelectric ceramics that actuate in the axial direction and generate two standing and bending waves with frequency f and phase difference α. The superposition of these two waves results in a travelling wave, moving the rotor via a friction layer. Usually, USMs are only driven by variations of the frequency f of the travelling wave. However, this prohibits the realization of low velocities, which can be achieved by additionally altering the phase difference α. We modified the motor controllers and proposed a novel hybrid SMC that is based on a dry friction driving principle of the motor and that realizes both low and high velocities. It controls frequency as well as phase difference and switches smoothly between the two control domains. Hence, a transition from low to high velocities, and vice-versa, cannot be felt by the operator. The key aspect in the control scheme is that no signum function has to be implemented, since it is already realized by the motor dry friction. This avoids chattering, otherwise typical for SMCs. The respective control scheme is depicted in Fig. 6 and shows how a desired joint position q_d is converted into motor commands.

First, the position error y_1 and velocity error y_2 are calculated. Then, a sliding surface S is created so that the system "slides" along the surface into the state $y_1 = 0$, $y_2 = 0$. Here, we use a linear sliding surface with $S = my_1 + y_2$. A subtraction of the rotor velocity $\dot{q}$ and the sliding surface S results in the control parameter μ. Via the two control laws $C_1(\mu)$ and $C_2(\mu)$, the phase difference α and the frequency f of the travelling wave can be controlled. The magnitude of the control parameter μ determines the control domain, which is either the phase difference or the frequency domain. This controller allows for

the position control of USMs with low velocities and smooth switching of the control domains.

The advantage of this new control principle is schematically depicted in the phase portrait in Fig. 7 that shows the motor's reaction to a position step input. A classical SMC (red) with a digitally implemented signum function follows an ideal linear slope S (dashed black) while oscillating around it. This oscillation continues when the origin of the phase portrait is reached. A nonhybrid SMC (dashed green), where the signum function is already part of the motor model and does not have to be implemented digitally, but that only uses the frequency to correct for position errors, cannot realize velocities lower than $\pm|v_{\text{min}}|$. Hence, it will also oscillate around the origin of the phase portrait. The proposed hybrid SMC follows a slope parallel to the ideal slope without oscillations and can switch to phase difference control to realize velocities below v_{min}. A steady-state error remains for this controller, and its magnitude depends on the slope m of the sliding surface S.

A more detailed description and evaluation of the controller can be found in our previous work [9].

V. HUMAN FACTORS ANALYSIS

A safe and ergonomic design is essential for the MR-Octo, since it is a tool for human motor control studies. This requires an analysis of the hardware and software components of the entire system. In order to design the haptic interface so that it is ergonomic and safe, we first analyzed the triplet users, use environments, and user interfaces. Then, we identified possible hazards via expert interviews as well as iterative prototyping and instantiated risk mitigation measures.

A. Description of Intended Device Users, Use Environments, and User Interfaces

The users, use environments, and user interfaces describe the setting in which the MR-Octo is employed. While the first two groups can only be influenced partially in the design process, a safe and ergonomic design can be realized via user interfaces.

1) Device Users: Typically, there are two groups of users of the MR-Octo. First of all, there are subjects participating in a human motor control study that are mostly naive to the use of haptic interfaces. Second, there are neuroscientists that design

Fig. 8. Main user interfaces of the MR-Octo for scientists (left) and subjects (right).
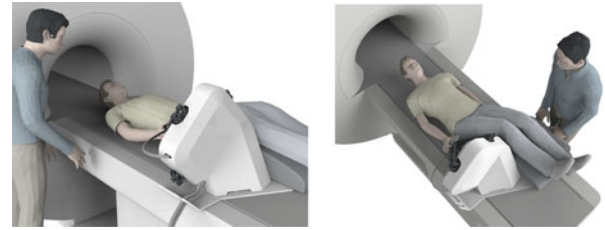

Fig. 9. Guided training of the subject (left) and adjustment of the position of the haptic interface to reach an ergonomic position (right).

and carry out fMRI studies with the device, but who are still not technical experts on every detail of the system.

2) Use Environments: The MR-Octo is designed for use in MR scanners. Hence, strong magnetic fields are expected and moreover, the subjects as well as the system share a small workspace. Additionally, noise levels during fMRI analyses are high. Verbal communication with the subject and auditory fault detection are not possible during the scans.

3) Device User Interfaces: There are three main user interfaces for the scientists employing the MR-Octo: First of all there are two handles on the support frame, such that the system can be carried by two persons, as depicted on the left in Fig. 8. The handles remain accessible to adjust the position of the system when a subject is lying on the scanner bed. Second, there are screws with knurling, in order to lock the position of the support frame on the scanner bed. Third, three cables are attached to the MR-Octo: one cable for the motors, one cable for the encoders, and one cable for the force/torque sensor with six DoF.

The subject has three points of interaction with the MR-Octo, as shown on the right in Fig. 8. The right hand grasps the haptic gripper, the legs are placed on an MRI pillow, and a virtual environment is displayed on a screen visible through a mirror on the head coil. Within the virtual environment, the subject can see if the MR-Octo is activated or not. With a switch at the gripper, the subjects turns the haptic interface on or off.

B. Analysis of Hazards and Risks Associated With the Device

We classify hazards and risks according to ISO 10218-2. Hazards resulting from a general fMRI scan without the MR-Octo are only listed if there is a relation to the haptic interface.

1) Mechanical Hazards:

a) Movement of the end effector and gripper may lead to crushing the hand between haptic interface and MR scanner: Countermeasures are a limited workspace, force/torque and velocity production, implemented in software, in order to reduce likeliness and severity of an impact.

b) Movement of the robot legs might lead to an impact on the subjects' legs: As a countermeasure, the support frame is designed in such a way that the subject's and robot's legs remain separated by a small wall.

c) Repeated plugging and unplugging of the nine motors and encoders might lead to mixed cables or cable breaks, and consequently to an uncontrolled motion of

the end effector due to faulty signals: As a countermeasure, two main cables bundle all motor as well as encoder signals, and plugs are from nonmagnetic metal and thus, robust.

d) The movement of the MR scanner bed might unplug the two cables for motors and encoders and either switch off the system unintentionally or lead to an uncontrolled motion of the end effector: As countermeasures, the connectors are secured via screws and cables are clamped on the support frame.

2) Electrical hazards:

a) Contact with live parts, such as connectors, can result in electrocution: As a countermeasure, a nonconducting chassis protects live parts and connections from contact with the environment.

b) During the installation of the system, the main cables for motors and encoders might be connected to the wrong slots at the MR-Octo and the filter box of the scanner room: This can result in damage to the encoders. As a countermeasure, plugs for motors and encoders are different and either female or male, respectively. Hence, the cables cannot be confused.

3) Thermal Hazards:

a) Hot surfaces associated with the MR-Octo may occur due to the RF pulses of the MR scanner and lead to burns: As a countermeasure, only nonmagnetic components that do not heat up are used on the outside of the haptic interface. Furthermore, no cables of the device are located close to the subject.

b) Surfaces of the USMs might heat up after long operation times: As a countermeasure, the chassis protects the motors from being touched from the outside.

4) Ergonomic Hazards:

a) An inappropriate location or identification of controls, i.e. the haptic gripper, may lead to unhealthy postures or excessive effort of the subject: As a countermeasure, the haptic interface can be adjusted on the scanner bed during training. To do so, the frame can be moved lengthwise and laterally. Hence, an ergonomic posture can be ensured, as depicted in Fig. 9.

b) An inappropriate location of controls may lead to unhealthy postures or excessive effort of the scientists while carrying the frame: As a countermeasure, handles that are easily accessible were added to the frame so that it can be carried with little effort. This is depicted on the left in Fig. 8.
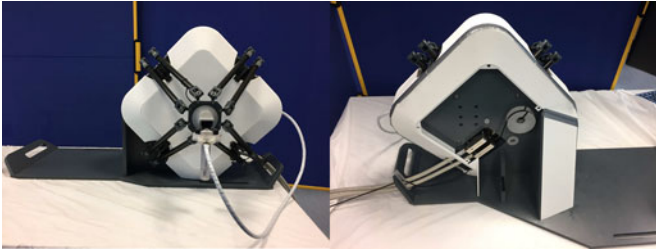
Fig. 10. Photographs of the MR-Octo from the front (left) and back (right). The backside can be closed entirely by the chassis, which is not depicted.

In conclusion, the remaining hazards and critical tasks in the scanner room, related to the MR-Octo system, were first of all identified via different methods. Then, they were addressed via countermeasures that ensure safety and an ergonomic handling of the system.

VI. EXPERIMENTAL VALIDATION

A first prototype of the device is validated and the successful implementation of the design requirements is quantified via performance indices. Photographs of the device are depicted in Fig. 10.

A. Performance Indices

The analysis of a range of performance indices led us to the design of an Octopod kinematics [7]. Here, we focus on the most important indices.

1) Worst-Case Output Capabilities: In order to verify whether our design criteria are met in terms of force, torque, velocity, and acceleration, the worst-case output capabilities are quantified. For actuation-redundant actuators, the problem is over-constrained and thus, we employ the "polytope algorithm" [7] from our previous work. The equations for the output capabilities are given by

$$\dot{\mathbf{x}} = \mathbf{J}^{\#} \dot{\mathbf{q}}, \tag{4}$$

$$\mathbf{f} = \mathbf{J}^{T} \boldsymbol{\tau}; \ \dot{\mathbf{q}} = \mathbf{0}, \tag{5}$$

$$\ddot{\mathbf{x}} = \mathbf{J}^{\#} \mathbf{M}_{q}(\mathbf{q})^{-1} \boldsymbol{\tau}; \ \dot{\mathbf{q}}, \mathbf{f} = \mathbf{0}, \tag{6}$$

where $\mathbf{J}^{\#}$ is the generalized Moore–Penrose pseudoinverse, defined as $\mathbf{J}^{\#} = (\mathbf{J}^{T}\mathbf{J})^{-1}\mathbf{J}^{T}$. These equations relate actuator capabilities, such as velocities $\dot{\mathbf{q}}$ and torques $\boldsymbol{\tau}$, to end effector capabilities, namely its velocities $\dot{\mathbf{x}}$, its wrench $\mathbf{f}$, and its accelerations $\ddot{\mathbf{x}}$. The relations build on the Jacobian $\mathbf{J}$ and the mass matrix in joint space $\mathbf{M}_{q}(\mathbf{q})$. The "polytope algorithm" consists of four steps, and allows for the obtaining of the worst-case translational and rotational output capabilities individually. This means that in the translational case, all rotational output capabilities are at zero magnitude, and vice versa. This means that e.g., pure force production capabilities can be calculated, where no residual torque is generated. Within the first step of the "polytope algorithm,' actuator capabilities, such as torque and velocity, are set to maximum and minimum, respectively. Using (4)–(6), the vertices of the polytope in the task space are
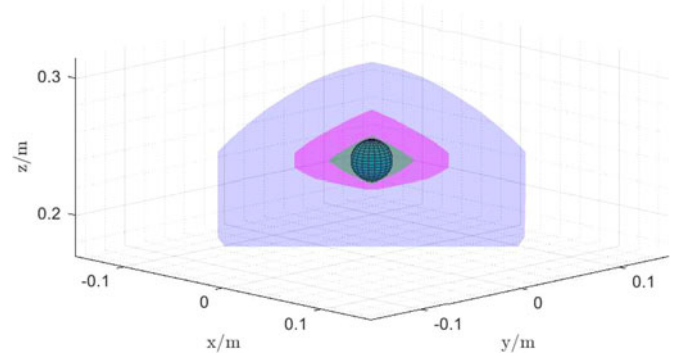

Fig. 11. Simulated reachable workspace with only translational displacements of the Octopod kinematics, depicted in blue and simulated dexterous workspace volumes, where $\pm 30°$ and $\pm 20°$ rotations around all axes are achievable shown in green and magenta, respectively.

computed. In a second step, the convex hull of the polytope is computed. Then, the polytope is sliced along the axes of the auxiliary condition in order to obtain pure translational or rotational output. Finally, the minimum distance to the surface is computed, resulting in the worst-case output capabilities.

2) Workspace: The dexterous workspace describes the maximum volume in which rotations in a certain range around all axes can be achieved. This volume is quantified along with the reachable workspace at zero rotations, as a comparison.

B. Results

1) Dexterous Workspace: The size of the dexterous workspace of the MR-Octo is mainly determined by physical joint limits and link lengths. The maximum volume, where rotations of $\pm 30°$ and $\pm 20°$ can be achieved around all axes, is shown in Fig. 11 as green and magenta volume, respectively. The reachable workspace at zero rotations is shown in blue. The dexterous workspace with $\pm 30°$ rotations around all axes is approximated with a sphere (S30), centered at $z = 0.24$ m and with a diameter of 30 mm, which is also depicted in Fig. 11. The dexterous workspace with $\pm 20°$ rotations around all axes is also approximated with a sphere (S20) with a diameter of 50 mm (not shown).

2) Worst-Case Output Capabilities: Via a theoretical and experimental evaluation of worst-case output capabilities, we verify whether the design goals in terms of minimum force, velocity and acceleration are met. The spherical workspaces S20 and S30 are sampled with a translational step size of 2 mm and a rotational step size of $10°$ in a range of $\pm 20°$ and $\pm 30°$ around all axes, respectively. The USMs produce a nominal torque of $\tau_{i,\max,n} = \pm 0.5$ Nm, a stall torque of $\tau_{i,\max,st} = \pm 1.0$ Nm, and a nominal velocity of $v_{i,\max,n} = \pm 10$ rad/s. The Cartesian mass matrix is approximated with the help of CAD data as $\hat{\mathbf{M}} = diag[m_{OC} \ m_{OC} \ m_{OC} \ I_x \ I_y \ I_z]$ with $m_{OC} = 0.05$ kg, $I_{x,y,z} = 3 \times 10^{-4}$ kgm^2, and the similarity transformation to joint coordinates $\mathbf{M}_{q}(q) = \mathbf{J}(\mathbf{q})^{T}\hat{\mathbf{M}}\mathbf{J}(\mathbf{q})$. The resulting worst-case output capabilities of the kinematics within the workspaces and considered allowed rotations around all axes are listed in Table III.

TABLE III
WORST-CASE OUTPUT CAPABILITIES OF THE MR-OCTO IN ITS DEXTEROUS
WORKSPACE AS WELL AS DESIRED VALUES

Output capability	Simulation		Experiment		Des.
	S20	S30	S20	S30	
Continuous force (N)	7.83	7.45	7.51	6.87	1.96
Continuous torque (Nm)	0.49	0.43	0.46	0.41	0.52
Velocity (m/s)	0.34	0.16	0.44	0.42	1.0
Angular velocity (rad/s)	8.53	6.78	14.09	13.82	–
Acceleration (m/s^2)	239.33	227.79	515.69	378.47	9.81
Angular Acc. (rad/s^2)	3302.30	2891.64	5726.61	4301.62	–

TABLE IV
WORST-CASE OUTPUT CAPABILITIES OF THE GRIPPER AS
WELL AS DESIRED VALUES

Output capability	Simulation	Experiment	Des.
Continuous force (N)	7.14	5.04	8.3
Velocity (m/s)	0.11	0.21	1.0

Fig. 12. Setup for force/torque sensor MR-compatibility test.

Additionally, the worst-case output capabilities of the gripper were evaluated and the results are listed in Table IV.

VII. MR-COMPATIBILITY VALIDATION

Finally, the MR-compatibility of the entire system was validated in order to ensure its applicability for fMRI analyses.

A. Validation Methods

The bi-directional MR-compatibility was validated in a 3 T MRI scanner (Prisma, Siemens Healthcare, Erlangen, Germany) equipped with a 20-ch Siemens head coil and a phantom filled with a saline water solution. The procedure was carried out in three major steps: In the first step, we used a double-echo gradient echo sequence to create a B_0 map without any device present. Then, with the device placed at the entry of the scanner bore and powered off, another B_0 map was recorded. This allowed for the verification that the device does not lead to distortions in the B_0 field that cannot be corrected by shimming. Then, in a second step and after shimming, radio frequency (RF) noise was measured with the device powered on and moving. In the third and last step, we ran an echo planar imaging (EPI) sequence, while the device altered between moving and holding its position in an ON/OFF block design. The signal-to-fluctuation-noise ratio (SFNR) that was calculated from EPI images, the RF noise spectrum and the signals recorded from the device were then used to determine the MR-compatibility.

1) Titanium Force/Torque Sensor With Six DoF: Using this procedure, the force/torque sensor with six DoF was validated individually, prior to an evaluation of the entire system. The Mini27 Titanium force/torque sensor with six DoF relies on a strain-gauge-based measurement principle that outputs an analogue signal. Hence, it is particularly susceptible to the magnetic field, in contrast to an optical measurement principle or a digital signal. Noise levels were determined to indicate whether filters, and thus delays, needed to be introduced or force dead zones had
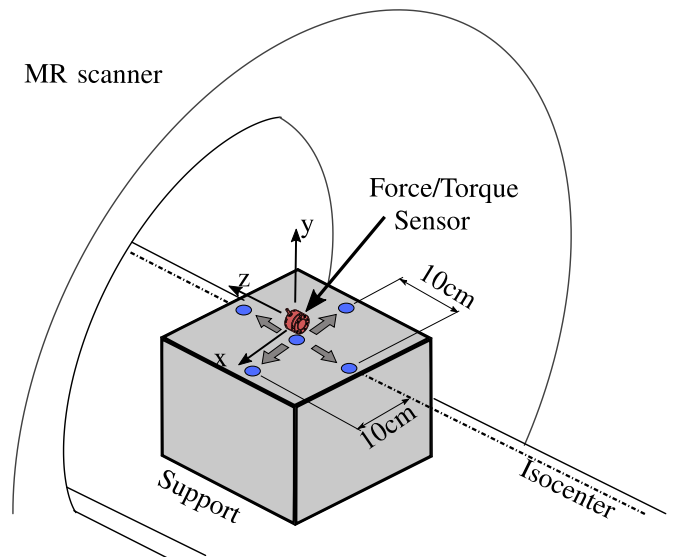
to be respected. The test setup at the entry of the MR scanner bore is depicted in Fig. 12.

The ATI was placed on a support so that it was in a comparable position to its later point of operation in the isocenter of the magnetic field. Since the sensor was not actuated, it was oriented and moved by hand in ranges that are comparable to the later workspace of the haptic interface. First, the sensor was in an upright position, as depicted in Fig. 12. Then, the sensor was tilted about $\pm30°$ around its *x*- and *y*-axis. Signals were recorded for 30 s in every orientation. The sensor was also placed in four different locations, each 10 cm away from the central position along the *x*-axis and the *z*-axis.

2) Haptic Interface: The MR-compatibility of the entire haptic interface was determined in a second step. To do so, the support frame was placed 12 cm from the scanner bore and the gripper was at a distance of 25 cm from the isocenter. The setup is depicted in Fig. 13. During the ON-blocks, the device moved sinusoidally along its *z*-axis with an amplitude of 2 cm and at 2 Hz. During the OFF-blocks, the haptic interface held its last position and motors were switched off.

B. Results

1) Titanium Force/Torque Sensor With Six DoF:

a) RF Noise Measurement and EPI Quality: The RF noise measurements show that there is no RF interference from the sensor leading to image artifacts. The mean and SFNR for the EPIs were also acquired when the sensor was turned off and on. The difference of the two states OFF and ON was calculated and no systematic variation or pattern could be found.

b) Impact of MRI on Sensor Signal Quality: The data was acquired at 1 kHz and noise from the scanner was found at 220 and 800 Hz. This finding is consistent across all tested positions and orientations. The width of the noise envelope is about 0.05 N in the center position and doubles when the sensor is moved 10 cm along the *z*-axis into the scanner. Finally, a dead
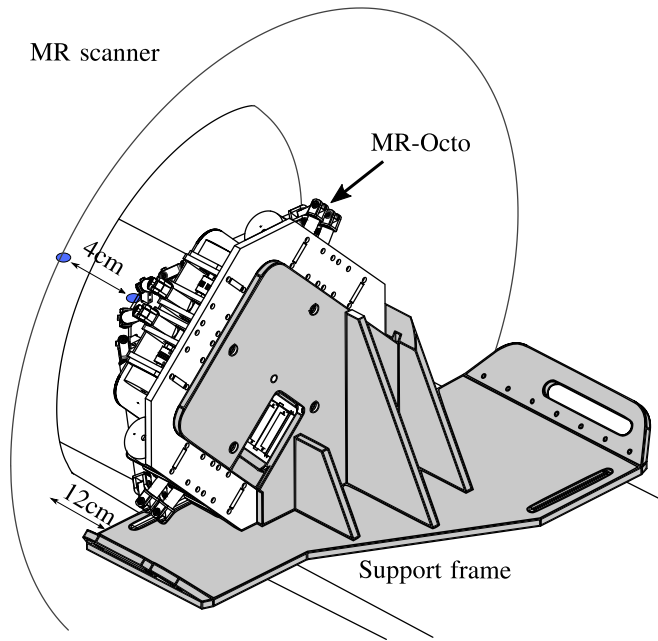
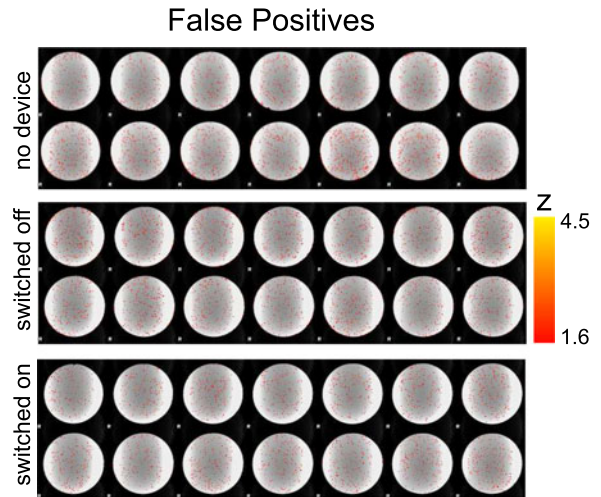Fig. 13.   Setup for MR-compatibility test of the MR-Octo.

Fig. 14.   The results of the GLM analysis for no device (top), the device switched off (middle), and switched on as well as moving (bottom). False positives in the background are absent due to an automatic masking procedure during the analysis.

zone of ± 0.1 N was introduced for force measurements and ± 0.05 Nm for torque measurements.

2) Haptic Interface:

a) RF Noise Measurement, Impact on B_0 Homogeneity and fMRI Quality: All of the compatibility measurements were carried out with a spherical testing phantom provided by the scanner vendor filled with distilled water that was doped with 1.25 g $NiSO_4 \times 6H_2O$ per 1000 g. The difference maps for the B_0 measurements revealed a general offset of up to 15 Hz between the case when the device was present in the bore versus the case without device. However, these changes are within the range of physiological effects (breathing changes the field up to 10 Hz) and were corrected by reapplying the shimming procedure of the scanner. The scanner vendor's RF noise measurement sequence was used to scan for background noise in a range of ± 250 kHz from the center frequency. It used the head coil for signal reception without any applied RF pulses or field gradients and scans for a duration of approximately 6 min. The mean noise for all three conditions, no device, device powered and device moving, matched very well with values of 39.61, 39.47, and 39.59, respectively, on an intensity scale from 0 to 4 095. In addition, the noise spectra for each condition did not show any increase of noise in the scanned frequency range. The signal-to-noise ratio (SNR) for each condition did not vary significantly, as expected from the conducted RF noise scans. The SNR-values were calculated by dividing the mean intensity of the voxels of the imaged phantom by the mean intensity of the background, which yielded 24.4, 25.5, and 25.1, respectively. The median temporal SNR for the three conditions is 253.5, 247.3, and 245.4. This translates to noise-to-signal ratios well below 1% and is similar to noise levels that were reported in [18].

The fMRI analysis was based on the general linear model (GLM) and was done with FSL 5.0 (FMRIB, Oxford University, U.K.). A high-pass cut-off of 120 s was chosen for the 30 s ON/OFF block design. In order to see voxel-level activation as well as an uncorrected z-map without spatial smoothing, thresholded statistical data with $p > 0.05$ was analyzed. Fig. 14 depicts the recorded data for three conditions, no device, device unpowered and the device switched on and alternating between performing a sinusoidal motion for 30 s and pausing for 30 s. The random distribution across the volume and the absence of clustering indicates no change of the pattern due to the presence of the moving device. Also, the percentage of false positives in the measured volume with a threshold z-score of 1.6 is 5.4%, 4.6%, and 3.8%, respectively, which matches the expected values for $p > 0.05$. Additionally, an independent component analysis (ICA) was performed on the data, which did not show any components correlated to the ON/OFF pattern or the sinusoidal movement.

b) Impact of MRI on the Tracking Capability: The tracking capability of the sinusoidal trajectory by the haptic interface is not impaired by the MRI. Performances during the scanning and outside the scanning room are indistinguishable and mean tracking errors are 0.04 mm both times.

VIII. Preliminary fMRI Study

In order to show the applicability of the device and to validate it, we carried out a preliminary fMRI study. In this work, we present the first results, but a thorough presentation of the entire study is beyond the scope of this paper.

Two subjects lifted objects of different weight. The grasp-and-lift (G&L) study was carried out both with the haptic interface (virtual G&L) and with a corresponding benchmark real-world object (benchmark G&L) with an attached sensor that allows for measuring grip forces. The data were synchronized by recording
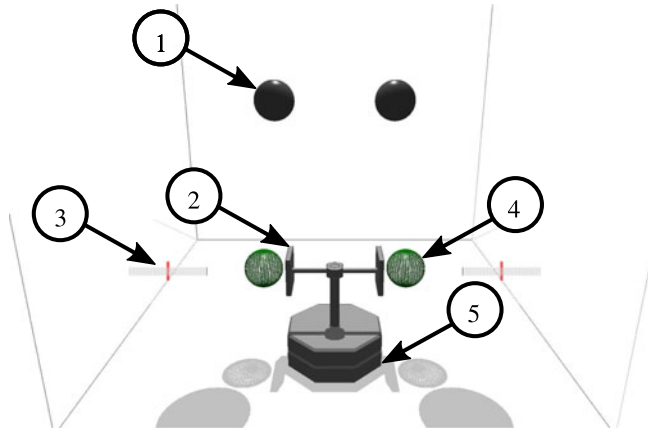
Fig. 15. Virtual environment showing (1) finger tip representations, (2) virtual object, (3) grasp force level bars, (4) rest positions, and (5) weight level.

Fig. 16. Thresholded *t*-maps of signal increases for virtual G&L (red), benchmark G&L (blue), and overlap (magenta). Left (L) and right (R) side are labeled in the first slice.

a trigger signal from the scanner that indicates the start of every echo-planar image (EPI) volume.

The study was approved by the ethics committee of the university hospital Tübingen and both subjects gave their informed consent. Subject one was left-handed, but highly trained on the MR-Octo.

A. Task Environment

The virtual environment used in conjunction with the MR-Octo is shown in Fig. 15. Virtual objects of four different weight levels are rendered and the level is indicated by the number of octagonal plates at the bottom of each object. The objects are grasped at a handle of constant width at the top. The applied grasp force is shown via two level bars.

In the case of benchmark G&L, the objects are 3D-printed, of same the weight and feature the same grip width. They can be seen via a mirror on the head coil that allows one to look out of the scanner bore.

B. Analysis and Results

The experiment was conducted on a 3 T MRI system (Prisma, Siemens; Erlangen, Germany) equipped with a 20-channel head coil. For the functional imaging, we employed gradient echo (GRE) EPI sequences (TR = 2 s, TE = 30 ms, FOV = 210×210 mm^3, flip angle = $74°$, voxel size = $2.5 \times 2.5 \times 2.5$ mm^3, and 50 slices). The functional data were motion-corrected offline and a T1 scan was coregistered to a mean functional scan. Anatomical and functional data were coregistered to MNI space. Functional scans were smoothed with a FWHM of 4 mm. For a voxel-wise whole brain analysis, we fitted a GLM to the measured data with arm and hand movement and measured peak grip forces as regressors of interest.

Subject one carried out eight runs of virtual G&L and six runs of benchmark G&L. Subject two conducted three runs of virtual G&L and six runs of benchmark G&L. Each run consisted of 300 EPI BOLD volumes and contained 32 trials. Each trial had a duration of 18 s, whereas the G&L movement took 2–4 s, followed by a resting period.
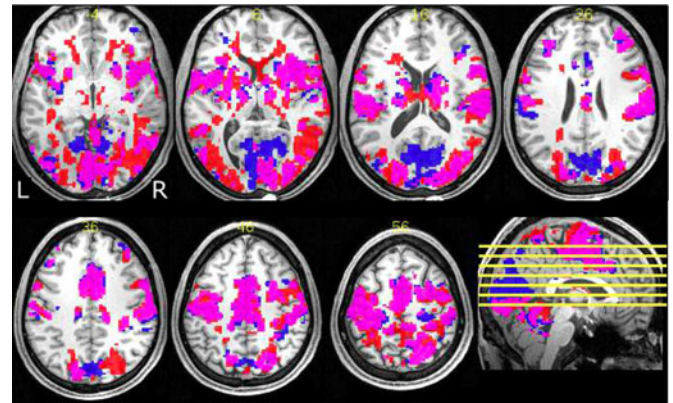
Fig. 16 shows *t*-maps of subject 1, thresholded with $p < 0.5$ (FWE-corrected for multiple comparisons) during virtual G&L in red, benchmark G&L in blue, and the overlap of both in magenta. The cortical and subcortical sensorimotor system is activated in both the cases with a large overlap between the conditions. The primary motor cortices in both the hemispheres as well as the medial visual cortex show stronger activations in the case of benchmark objects. The lateral visual cortex, on the other hand, is more active in the case of virtual G&L.

IX. DISCUSSION

Our design requirements in terms of actuated DoF are met and rotations of $\pm30°$ can be achieved in the dexterous workspace with a volume of 14137 mm^3. The desired minimum output capabilities in terms of force and acceleration are also achieved. The worst-case grip force is at 61% of the desired value. Worst-case torque and velocity in the dexterous workspace S30 are at 79% and 42% of their desired values, respectively. This reflects the typical compromise between force/torque and velocity capabilities that has to be made given a certain set of actuators. We reduced the worst-case velocity capability for the sake of force and torque production during the design process, since we expect force production tasks to be more frequent than tasks with very rapid movements. This reduction of worst-case velocity capability increases the worst-case force to 79% in the S30. Otherwise, it would be even lower. Moreover and as shown by the experimental results, the USMs can produce higher velocities than simulated for short amounts of time. Besides, with rotations of $\pm20°$, a 360% larger workspace can be covered and worst-case output capabilities increase to the values given in Table III. If required, the design of the haptic interface also allows one to easily change the link lengths and thus to adapt the haptic interface to velocity-focused tasks, if necessary. Since USMs have been employed in a broad variety of MR-compatible devices [2], [5], the MR-compatibility of our device is not surprising. However, our device contains the largest number of USMs, nine in total, ever tested to the best of our knowledge. Individual structural components or sensors that may have also interfered with the MR environment have been shown to have no

significant impact at the test position in the MR scanner. Hence, MR-compatibility can be concluded for this case.

We also designed a preliminary fMRI study that allows for the validation of the MR-Octo and quantification of in how far an MR-compatible haptic interface can render a virtual and haptic environment that leads to similar cerebral activations as a real-world scenario. A large overlap of cerebral activations in terms of voxels could be found. However, the visual cortex is more active in the case of virtual G&L. Hence, grasping and lifting virtual objects demands more visual data processing. This results most likely from the fact that force is mainly controlled visually using the level bars in the virtual environment.

X. CONCLUSION

In this work, we presented the first universal haptic interface for fMRI studies in the field of human motor control. It endows neuroscientists with a tool that can be reprogrammed and does not have to be redesigned when moving on to a new research question. Natural pick-and-place motions of light objects can be targeted with this device. The presented analysis shows the MR compatibility of the developed system in a 3 T scanner as well as a preliminary fMRI study. Future work will be directed toward conducting further human motor control studies.

ACKNOWLEDGMENT

REFERENCES

[1] M. A. Ergin, M. Kühne, A. Thielscher, and A. Peer, "Design of a new MR-compatible haptic interface with six actuated degrees of freedom," in *Proc. IEEE Int. Conf. Biomed. Robot. Biomechatronics*, 2014.

[2] S. Klare, A. Peer, and M. Buss, "Development of a 3 DoF MR-compatible haptic interface for pointing and reaching movements," in *Proc. Int. Conf. Humans Haptics: Generating Perceiving Tangible Sensations*, 2010, pp. 211–218.

[3] B. Vigaru, J. Sulzer, and R. Gassert, "Design and evaluation of a cable-driven fMRI-compatible haptic interface to investigate precision grip control," *IEEE Trans. Haptics*, vol. 9, no. 1, pp. 20–32, 2016.

[4] I. Farkhatdinov, A. Garnier, and E. Burdet, "Development and evaluation of a portable MR compatible haptic interface for human motor control," in *Proc. World Haptics Conf.*, 2015 [Online]. Available: http://ieeexplore.ieee.org/lpdocs/epic03/wrapper.htm?arnumber=7177713

[5] F. Sergi, A. C. Erwin, and M. K. Omalley, "Interaction control capabilities of an MR-compatible compliant actuator for wrist sensorimotor protocols during fMRI," *IEEE/ASME Trans. Mechatronics*, vol. 20, no. 6, pp. 2678–2690, Dec. 2015.

[6] S. Menon, A. Soviche, J. Mithrakumar, A. Subbarao, H. Ganti, and O. Khatib, "Haptic fmri: A novel five dof haptic interface for multi-axis motor neuroscience experiments," in *Proc. World Haptics Conf.*, 2017.

[7] M. Kühne, J. Potzy, R. García-Rochín, P. van der Smagt, and A. Peer, "Design and evaluation of a haptic interface with octopod kinematics," *IEEE/ASME Trans. Mechatronics*, vol. 22, no. 5, pp. 2091–2101, Oct. 2017.

[8] Z. Najdovski, S. Nahavandi, S. Member, and T. Fukuda, "Design, development, and evaluation of a pinch–grasp haptic interface," *IEEE Trans. Mechatronics*, vol. 19, no. 1, pp. 45–54, Feb. 2014.

[9] M. Kühne, R. G. Rochín, R. S. Cos, G. R. Astorga, and A. Peer, "Modeling and two-input sliding mode control of rotary traveling wave ultrasonic motors," *IEEE Trans. Ind. Electron.*, to be published.

[10] R. Gassert, E. Burdet, and K. Chinzei, "MRI-compatible robotics," *IEEE Eng. Med. Bio. Mag.: Quart. Mag. Eng. Med. Bio. Soc.*, vol. 27, no. 3, pp. 12–14, May–Jun. 2008. [Online]. Available: http://www.ncbi.nlm.nih.gov/pubmed/18519180

[11] J. C. Culham, C. Cavina-Pratesi, and A. Singhal, "The role of parietal cortex in visuomotor control: What have we learned from neuroimaging?" *Neuropsychologia*, vol. 44, no. 13, pp. 2668–2684, 2006. [Online]. Available: http://www.ncbi.nlm.nih.gov/pubmed/16337974

[12] P. Fischer and R. Daniel, "Specification and design of input devices for teleoperation," in *Proc. IEEE Int. Conf. Robot. Autom.*, 1990.

[13] W. Karwowski, *International Encyclopedia of Ergonomics and Human Factors*. Boca Raton, FL, USA: CRC Press, 2006.

[14] G. Westling and R. S. Johansson, "Factors influencing the force control during precision grip," *Exp. Brain Res. Experimentelle Hirnforschung. Experimentation Cerebrale*, vol. 53, no. 2, pp. 277–284, 1984.

[15] G. Cadoret and A. M. Smith, "Friction, not texture, dictates grip forces used during object manipulation," *J. Neurophysiology*, vol. 75, no. 5, pp. 1963–1969, 1996.

[16] S. Tomlinson, R. Lewis, and M. Carre, "Review of the frictional properties of finger-object contact when gripping," *Proc. Inst. Mech. Eng., Part J: J. Eng. Tribology*, vol. 221, pp. 841–850, 2007.

[17] F. Conti *et al.*, "The CHAI libraries," *Eurohaptics*, 2003.

[18] S. Menon, H. Ganti, and O. Khatib, Using Haptic fMRI to Enable Interactive Motor Neuroimaging Experiments *Using Haptic fMRI to Enable Interactive Motor Neuroimaging Experiments* (Springer Tracts in Advanced Robotics: Experimental Robotics). Netherlands: Springer, 2014.

Markus Kühne received the Diploma Engineering degree in mechanical engineering from the Technical University of Munich, Munich, Germany, in 2013; the Diploma Engineering degree in robotics and embedded systems from École Nationale Supérieure de Techniques Avancées ParisTech, Paris, France, in 2012; and the Master's degree in robotics from the Université Pierre et Marie Curie, Paris, France, in 2012. He is currently working toward the Doctor of Engineering degree in electrical engineering at the Technical University of Munich.

His research interests include robot design and control as well as medical robotics.

Martin Eschelbach received the Diploma degree in physics from Eberhard-Karls-Universität Tübingen, Germany, in 2013. He is currently working toward the Ph.D. degree at the Max-Planck-Institute for Biological Cybernetics, Tübingen, Germany.

He was as an Intern in financial consulting.

Ali Aghaeifar received the B.Sc. degree in biomedical engineering from Amirkabir University of Technology, Tehran, Iran, in 2010, and the M.Sc. degree in electrical engineering from Iran University of Science & Technology, Tehran, Iran, in 2012. He is currently working toward the Ph.D. degree in neuroscience at the Max-Planck-Institute for Biological Cybernetics, Tübingen, Germany.

His research interests include prospective motion correction and dynamic shimming in MRI.

Lisa von Pflugk studied integrated product design at the University of Applied Sciences and Arts, Coburg, Germany. For her Bachelor's thesis, she specialized in medical design. She received the M.Sc. degree in industrial design from the Technical University of Munich, München, Germany, in 2017.

She has worked with Siemens Healthineers (formerly Siemens Healthcare) and focused on patient handling and the workflow within CT examinations. She is currently working as an Innovation Consultant and Designer with the Institute for Innovation and Change Methodologies, Munich, Germany.

Axel Thielscher obtained the Doctoral degrees in electrical engineering and biomedical sciences from the University of Ulm, Ulm, Germany), and the Postdoc degree from Brown University, Providence, RI, USA.

He was a Research Group Leader with the Max-Planck-Institute for Biological Cybernetics, Tübingen, Germany. He currently holds a shared position as an Associate Professor at the Danish Research Center for Magnetic Resonance, Hvidovre, Denmark, Copenhagen University Hospital Hvidovre, Hvidovre, Denmark, and the Technical University of Denmark, Kgs. Lyngby, Denmark. His research interests include the biophysics of transcranial brain stimulation, combined neurostimulation-neuroimaging approaches, and the application of these methods to study human sensorimotor integration and motor control processes.

Marc Himmelbach received the Diploma degree in psychology from Heinrich Heine University Düsseldorf, Düsseldorf, Germany and the Doctoral degree in neural and behavioural sciences from Eberhard-Karls-University of Tübingen, Tübingen, Germany, in 2000 and 2005, respectively.

He is currently working as a Postdoc Researcher at the Center of Neurology, and established a research group on Neuropsychology of Action Control, Hertie Institute for Clinical Brain Research, Tübingen, Germany, in 2008.

Dr. Himmelbach received the ERC Starting Grant in 2007.

Klaus Scheffler received the M.S. degree in theoretical physics from the University of Freiburg, Freiburg, Germany, in 1992, and the Ph.D. degree in biophysical chemistry from the University of Basel, Basel, Switzerland, in 1995.

He worked as a Postdoc Researcher and a Research Scientist with MR-Center and Biocenter, University of Basel. In 1995, he joined the Department of Medical Physics, University of Freiburg, as a Research Group Leader. In 2002, he was promoted to Assistant Professor, in medical physics, by the Swiss Federal Science Program, University of Basel, and in 2003, he received a Research Award Professorship from the Swiss National Science Foundation. In 2011, he was appointed as a Full Professor (W3-Chair) and the Director of the Department of Neuroimaging, Werner Reichardt Center for Integrative Neurosciences, University of Tübingen, and became the Max Planck Fellow and Head of the MRC-Department, Max Planck Institute for Biological Cybernetics, Tübingen, Germany.

Patrick van der Smagt received the Ph.D. degree in mathematics and computer science from the University of Amsterdam, Amsterdam, Netherlands.

He is a Director of A I Research at Volkswagen Group, Munich's Data Lab, München, Germany. He was a Professor for machine learning and biomimetic robotics at the Technical University of Munich, and was the Head of bionics and assistive robotics at the DLR Oberpfaffenhofen. He has published numerous papers and patents on machine learning, robotics, and motor control. His research interests include unsupervised stochastic deep and recurrent models, time series modeling, optimal control, robotics, and quantum computing.

He has received the 2013 Helmholtz-Association Erwin Schrdinger Award, the 2014 KingSun Fu Memorial Award, the 2013 Harvard Medical School/MGH Martin Research Prize, and various Best Paper Awards. He is founding Chairman of a non-profit organization for assistive robotics for tetraplegics and a Cofounder of various companies.

Angelika Peer received the Diploma Engineering degree in electrical engineering and information technology and the Doctor of Engineering degree both from the Technical University of Munich, Munich, Germany, in 2004 and 2008, respectively.

She is currently a Full Professor with the Free University of Bozen-Bolzano, BZ, Italy. From 2014 to 2017, she was a Full Professor at the Bristol Robotics Laboratory, University of the West of England, Bristol, U.K. Previously, she was a Senior Researcher and a Lecturer at the Institute of Automatic Control Engineering and a TUM-IAS Junior Fellow of the Institute of Advanced Studies, Technical University of Munich, München, Germany. Her research interests include robotics, haptics, teleoperation, human–human and human–robot interaction, and human motor control.